Available online at www.sciencedirect.com
ScienceDirect
Trans. Nonferrous Met. Soc. China 35(2025) 30−44
Transactions of Nonferrous Metals Society of China
www.tnmsc.cn

Influence of symmetric and asymmetric rolling on texture evolution of work-hardened AA 5xxx aluminium alloy

Matjaž GODEC[1], Stefan ZAEFFERER[2], Jakob KRANER[1,3], Črtomir DONIK[1], Irena PAULIN[1]

1. Institute of Metals and Technology, Lepi pot 11, 1000, Ljubljana, Slovenia;
2. Max-Planck-Institut für Eisenforschung, Max-Planck-Strasse 1, 40237 Düsseldorf, Germany;
3. Impol 2000 d.d., Partizanska cesta 38, 2310 Slovenska Bistrica, Slovenia

Received 30 May 2023; accepted 28 December 2023

Abstract: The textures and microstructures of hot- and cold-rolled sheets of an AA 5454 aluminium alloy were studied, with special attention paid to comparing the texture development for the symmetric and asymmetric cold rolling. Scanning electron microscopy with electron-backscatter diffraction was used to monitor the development of the microstructure in the differently deformed and additionally annealed samples. Details of the formations and transformations of individual texture components occurring during the rolling processes were observed and discussed. The average grain sizes, textures and mechanical properties were correlated and explained for the symmetric and asymmetric cold-rolled samples. The asymmetric rolling is beneficial in terms of deep drawability because it reduces the planar anisotropy of the annealed material due to the decrease of the Cube, Goss, rotated-Cube and η-fibre texture components and at the same time strengthens $X1$- and $X2$-fibre texture components which are shear texture components and improve deep drawability. During the asymmetric cold rolling, the temperature increases due to friction, triggering recrystallisation processes and leading to larger grains. It is also confirmed that asymmetric cold rolling uses less rolling force and consequently less energy to produce a final material with better formability, particularly earing.
Key words: crystallographic texture; EBSD; aluminium alloy; symmetric/asymmetric rolling; anisotropy

1 Introduction

The properties of metals and alloys are largely determined by three factors: chemistry, microstructure, and texture. Although the influence of texture is generally a second-order effect, it is crucial for the optimisation of many technical products, as texture determines the anisotropy of the properties of polycrystalline materials [1]. Depending on the deformation and annealing processes, aluminium alloys tend to form strong textures with large variability. Most of these textures are undesirable because they limit the deformability and the isotropy of the deformation behaviour [2]. Unfortunately, texture cannot be completely avoided in aluminium alloys, but it can be controlled to minimise its effects [3]. Aluminium alloys have an fcc crystal structure and a high stacking-fault energy (SFE). Therefore, their rolling and recrystallisation textures mainly follow the well-known Copper-type behaviour [4]. Nevertheless, due to the particularly high SFE of aluminium alloys, the relatively high homologous temperature (T/T_m, with T being the rolling temperature and T_m the melting temperature in Kelvin) and the important role of precipitations, the rolling and recrystallisation textures exhibit certain characteristics [5]. The high SFE causes a particular cold-rolling texture: the β-fibre (Brass−Copper−S)

Corresponding author: Matjaž GODEC, E-mail: matjaz.godec@imt.si
https://doi.org/10.1016/S1003-6326(24)66663-X

(see Tables 1 and 2 for the crystallographic definition of the different texture components) tends to occupy the S component, while the Brass and Copper components are weak [6]. The high SFE is also responsible for forming a strong Cube texture during recrystallisation after heavy cold rolling, provided the extent of the precipitation is low [7,8]. When the precipitation or the number of slowly diffusing alloying elements (e.g., Mn) is high, in contrast, grain-boundary pinning during the recrystallisation suppresses the formation of the Cube texture and creates a weak retained rolling texture. Rolling at high temperatures leads to a complex texture evolution because the thermal (recovery and recrystallisation) and athermal (dislocation movement and related lattice rotations) processes are superimposed [9]. Recrystallisation processes usually support a Cube texture, while shear processes caused by friction on the rollers during hot rolling lead to the Brass texture [10,11]. The latter is caused by a crystal rotation from the Cube via Goss to Brass. Consequently, the Cube−Goss η-fibre and the Goss−Brass α-fibre are formed. The Brass texture plays a role during the deformation of fcc alloys: it develops most strongly in materials with low stacking-fault energy where strong planar slip and/or deformation twinning prevails. This deformation behaviour limits the number of available slip systems and promotes shear banding [12]. In turn, the lattice rotation inside the shear bands leads to the Brass orientation [13]. Similar behaviour occurs during hot rolling when severe friction promotes shear banding.

The 5xxx Al alloys (containing Mg and Mn) are non-ageable, corrosion-resistant alloys with good strength. However, a relatively weak deep drawability frequently limits their applications. The texture components and intensities of alloy heavily influence the material properties; therefore, crystallographic texture analysis is crucial [14]. For our material and processing, the texture components can be classified into three groups, i.e., plane-strain (PSC), shear (SC) and recrystallisation (RXC), and each of them includes various texture components. The components of the plain-strain class are Copper, S, Brass and Goss, where the last two can also be a consequence of shear or recrystallisation during hot rolling. The shear class consists of the Brass and the rotated-Cube texture components. The recrystallisation class, finally, is composed of the Goss and Cube-texture components. HIRSCH and AL-SAMMAN [15] pointed out that the Cube component is the most prominent and common recrystallisation texture component in the fcc crystal system with a high-to-medium SFE. It originates from a classic nucleation mechanism [16]. Besides the Cube-texture component, LI et al [17] mention the Brass, S, Copper, Rotated-Cube and Goss as relevant texture components in 5xxx Al alloys.

The deep drawability of aluminium alloys can be improved by strengthening the γ-fibre [18], which can be developed with an additional step of warm rolling [19]. Different authors reported that formability and deep drawability could be improved with asymmetric rolling (ASR) as a metal-forming process [20,21]. In the literature, better mechanical properties (formability and deep drawability) in conjunction with asymmetric rolling are associated with a larger number of shear texture components [22,23] and more random texture [24]. For example, van HOUTTE et al [25] presented an increased

Table 1 Crystallographic data for texture components used in analyses

Texture component	Crystallographic plane and direction, $\{hkl\}\langle uvw\rangle$	Euler angle/(°)			Number of components	Group*
		φ_1	Φ	φ_2		
Cube	{001}⟨100⟩	0	0	0	1	RXC
Goss	{011}⟨100⟩	0	45	0	2	PSC and RXC
Brass	{011}⟨211⟩	35	45	0	2	SC and PSC
Copper	{112}⟨111⟩	90	35	45	4	PSC
S	{123}⟨634⟩	59	34	65	4	PSC
Rotated-Cube	{001}⟨110⟩	45	0	0	1	SC
Random	All other identified texture components					

* Groups are plane strain (PSC), shear (SC), and recrystallisation (RXC); All spherical texture components have orthotropic symmetry, and fibre texture component has monoclinic symmetry

Table 2 Crystallographic data for fibres used in analyses

Fibre texture component	Fibres path crystallographic description	Group
*X*1	$\langle 001\rangle_c \| \| [\bar{1}02]_s$	SC
*X*2	$\langle 001\rangle_c \| \| [102]_s$	SC
η-fibre	$\langle 001\rangle_c \| \| [100]_s$	SC

amount of *γ*-fibre in an ASR material and, at the same time, an equivalent decrease in the amount of *β*-fibre. JEONG et al [26] showed that the texture changes of a 7075 aluminium alloy were more evident after heat treatments. In contrast, the texture changes caused by a single asymmetric rolling pass were never investigated to the best of our knowledge. Consequently, details of the relations between the texture changes and the shear microstructures caused by ASR are still unknown.

In this work, we report on the texture changes caused by a single pass with a strain of 33% applied to a hot-rolled AA 5454 alloy with a relatively low texture intensity. The applied cold rolling was either symmetric or asymmetric with a single rolling pass. The resulting materials were further annealed to investigate the effect of complete recrystallisation on the deformation textures. The mechanical properties, including normal and planar anisotropy, were measured for all the rolled and recrystallised materials. These data are discussed in terms of the amount of random, shear texture created by the thermo-mechanical processing, as well as a microstructure analysis and the energy consumption related to asymmetric and symmetric cold rolling.

2 Experimental

Plates sized 510 mm × 230 mm × 6.7 mm of the industrial hot-rolled AA 5454 (EN AW-5454) aluminium alloy (composition of 2.43 wt.% Mg, 0.61 wt.% Mn, 0.25 wt.% Fe, 0.18 wt.% Si, 0.09 wt.% Cr, and balanced Al) were symmetrically and asymmetrically cold rolled. The details of the metallurgical process were: homogenization in the industrial furnace with ingot dimensions of 5500 mm × 1150 mm × 510 mm and regime of (590±10) °C for (6±0.5) h; industrial hot rolling on the reverse-quarto mill with entry thickness of (510±1) mm, exit thickness of (6.7±0.02) mm, temperatures of (505±10) °C at discharging, (480±10) °C before first pass, (365±10) °C before last pass with 19 passes (3 coiling passes) and average rolling force of (15580±50) kN with an average rolling speed of (120±12) m/min, average entry tension of (12±2) N/mm^2 and average exit tension of (17±2) N/mm^2. The symmetric cold rolling on the duo-laboratory mill was performed using 1 pass with a roll gap high set on 4.5 mm; factor of asymmetry was 1.0; entry thickness was (6.7±0.02) mm and exit thickness was (4.9±0.02) mm; max rolling force used was (1130±5) kN with max rolling torque of (5540±10) N·m. The asymmetric parameters were 1 pass with a roll gap high set on 4.5 mm; factor of asymmetry was 1.5; entry thickness was (6.7±0.02) mm and exit thickness was (4.9±0.02) mm; max rolling force was (1100±4) kN with max rolling torque of (6040±12) N·m. A duo laboratory mill was used to apply a thickness reduction of 33% in a single pass. The asymmetry ratio was calculated as the velocity quotient between upper and bottom rollers. In the symmetric rolling, the asymmetry ratio was 1.0, indicating the rollers had the same rotation speeds. The as-rolled material was used as a reference. An asymmetry ratio of 1.5 was achieved, with the bottom roller velocity at 0.33 r/min. The rollers diameter was 295 mm. Annealing in the laboratory furnaces was performed with a regime of (400±10) °C for (1±0.02) h (cooled in the air).

The sample labelling is listed in Table 3. Samples for light microscopy (LM) and scanning electron microscopy (SEM) were ground to 320 grit, polished with diamond and finished with 10 min OP-S (oxide polishing suspension). An electrolytic etching with HF (5 mL HF and 100 mL H_2O) for 30 s at 40 °C, with 30 V and 0.5 mA, was used for the LM samples, which were subsequently observed with polarised light. Ion polishing with a PECS Gatan 628 for 50 min was used for the SEM−EBSD samples. EBSD mapping, Brinell hardness testing and average grain size measurements were performed on the top, centre and bottom of sample cross-sections. The average grain size on LM micrographs were measured according to the ASTM E112–13 (intersection method). For the EBSD mapping, a Zeiss CrossBeam 550 field-emission scanning electron microscope (FE-SEM), with an EDAX Hikari Super EBSD camera with APEX software was employed with a step size of 1 μm. The analyses were performed on 70°-tilted samples at a 15 kV accelerating voltage and a 10 nA probe current. EBSD post-processing was carried

out using OIM 8.6 software to calculate and represent the inversed pole figure maps in the *Z*-direction (IPF-*Z* maps), orientation distribution functions (ODFs) and pole figures (PFs) obtained from the EBSD measurements.

Table 3 Sample labelling

Sample	Description
HR	Hot rolled
SCR	Symmetric cold rolled
ACR	Asymmetric cold rolled
SCR+A	Symmetric cold rolled and annealed
ACR+A	Asymmetric cold rolled and annealed

The mechanical properties were measured using an Instron 8802 tensile-test machine. The tests were carried out at a strain rate of 0.0067 s^{-1} to fracture (a dogbone-shaped rectangle with a width of 12.5 mm and gauge length of 50 mm). The formability and plastic anisotropy were measured by determining the Lankford factor (r), which is the ratio of the true strain in the width and thickness of sheet ($r=\varepsilon_w/\varepsilon_t$). The measurements were performed with a load of 2 MPa, which created 15% of the tensile strain. The testing speed was 0.0067 s^{-1}, following the ASTM E517 standard. To evaluate the sheet's anisotropy, tensile samples (a simple strip-shaped rectangle with a gauge width of 20 mm and gauge length of 50 mm) were cut out of the sheet at 0°, 45° and 90° relative to the rolling direction (as for the classic tensile test ASTM E8 M). With the obtained r ratios of true strain in width and thickness, the normal anisotropy r_m is calculated according to the equation:

$$r_m=\frac{(r_0+2r_{45}+r_{90})}{4} \tag{1}$$

and the planar anisotropy Δr, with the equation:

$$\Delta r=\frac{(r_0-2r_{45}+r_{90})}{2} \tag{2}$$

where r_0, r_{45} and r_{90} denote the anisotropies at 0°, 45° and 90° relative to the rolling direction.

The cups for the earing test were extracted with an Erichsen 134 Model machine. Then, anisotropy determinations of the cups' ear measurements were performed on an Erichsen 126 PLUS device.

The texture analysis is exclusively based on EBSD data from sample areas of about 2.76 mm^2. The textures were calculated for each sample on three randomly selected areas of 844 μm × 1089 μm in the middle (centre) and on the surface (edge) of aluminium sheet cross-sections. The middle measurements were right in the centre of the aluminium cross-section, while the surface measurements refer to an area selected from the top surface (≤10 μm from the edge) of every analysed sheet. The initial hot-rolled material contained about 400 grains on this surface, which did not show any significant orientation clustering. The ODF was calculated using a series expansion over spherical harmonic functions up to a series expansion rank of 22, using cubic crystal symmetry (aluminium) and triclinic sample symmetry. The latter was used in order to apply the same analysis for the data from symmetric and asymmetric rolling. Nevertheless, for a volume determination of the texture component, the orthotropic symmetry of the symmetrically rolled samples was considered using a selection of all the symmetrically equivalent rolling-texture components.

The texture components Brass and Goss form the α fibre ⟨011⟩||ND, the texture components Brass, Copper, and S form the β fibre, and the texture components from Cube to Goss form the η fibre. Some texture components are marked in the {001}, {011} and {111} pole figures (Fig. 1(a)) and in the ODF sections of selected angles (Fig. 1(b)). In addition to these components with orthotropic symmetry, two additional typical shear components with monoclinic symmetry were selected to deal with the monoclinic symmetry of the asymmetric rolling process, i.e., the fibres called *X*1 and *X*2. Not mentioned in the literature, these texture fibres correspond to crystals inclined in the positive and negative shearing directions of ND-RD plane. Both components are found on the surfaces of the S component and most probably develop out of S when a strong shear-band deformation prevails. They are also marked in the pole figures (Fig. 1(a)) and in the ODF plot (Fig. 1(b)). Both fibres exist in the asymmetrically rolled samples. A fibre texture component η is also presented.

We determined the area (= volume) fraction of the components with a spread of 10° around the centre orientation for an analysis of the texture component's intensity that gives the best peak separation. We report this volume fraction as the

sum over all the symmetrically equivalent variants of the respective component. Additionally, there are varying volume fractions of grains that do not belong to any of the analysed components for different materials. This more-or-less randomly distributed background is reported as well. Furthermore, we report the percentage that every texture component occupies with respect to the total volume of all the analysed texture components.

3 Results

3.1 Initial material

The texture and microstructure of the initial, hot-rolled (HR) material are shown in Figs. 2 and 3. The material shows a heterogeneous distribution of

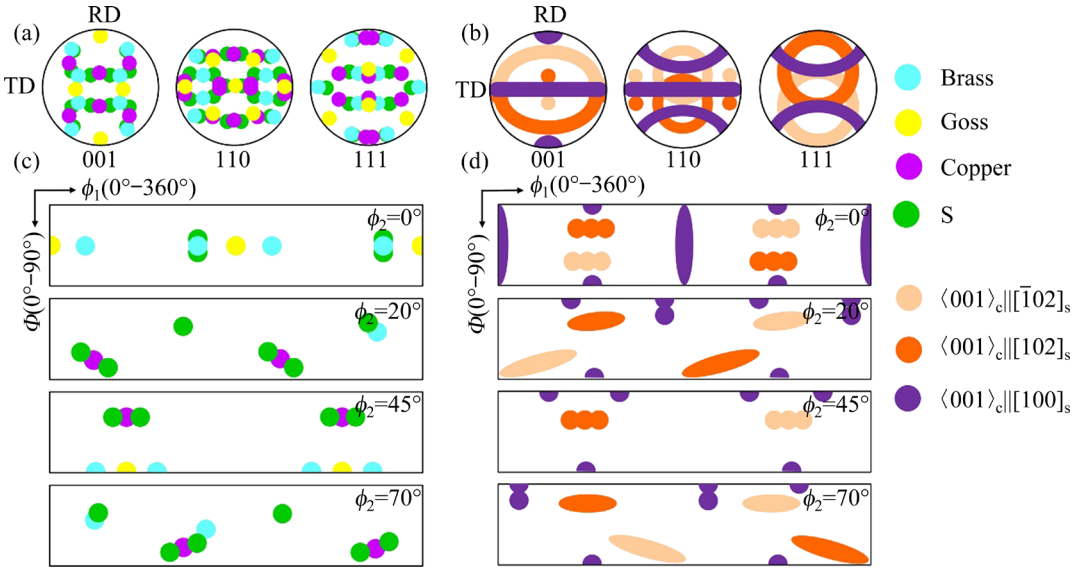

Fig. 1 Schematic of most important spherical and fiber texture components of material in pole figures (001, 110 and 111) (a) and Euler space at constant sections of ϕ_2 (b) (0°, 20°, 45°, 70°) [2, 4, 20]

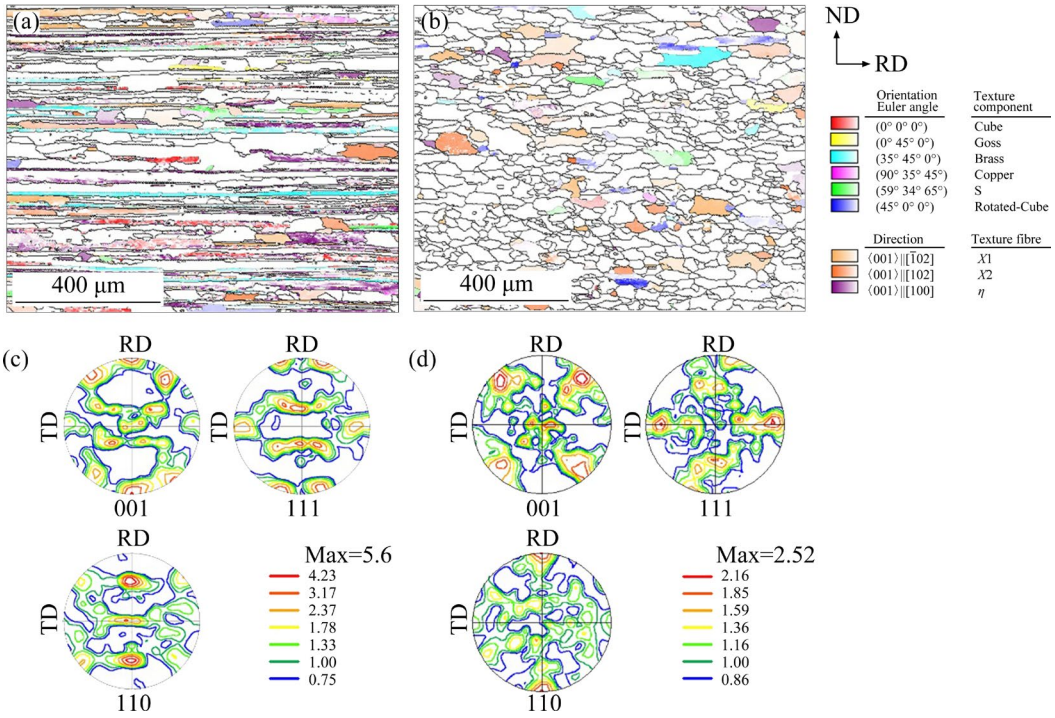

Fig. 2 Microstructure and texture of initial (hot-rolled) material, as observed by EBSD-based orientation mapping: (a) Composite image of spherical and fiber texture components, and grain boundaries in middle position of sample cross-section, consisting of pancake-shaped grains only; (b) Composite image of spherical and fiber texture components, and grain boundaries for position close to surface of sample cross-section, consisting of recrystallized grains only; (c) Pole-figure texture representation of middle area; (d) Pole-figure texture representation of area close to surface

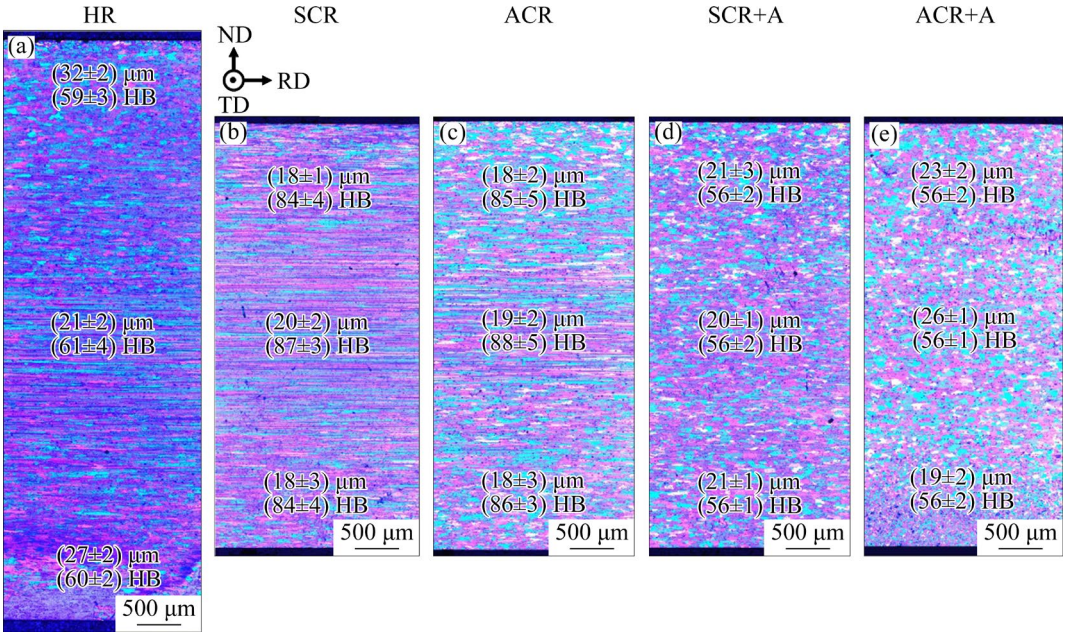

Fig. 3 LM microstructures with average grain sizes and Brinell hardness at top, bottom and centre positions in cross-section: (a) Hot-rolled (HR); (b) Symmetrically cold-rolled (SCR); (c) Asymmetrically cold-rolled (ACR); (d) Symmetrically cold-rolled and annealed (SCR+A); (e) Asymmetrically cold-rolled and annealed (ACR+A)

grain sizes with equiaxed recrystallised grains in the outer thirds of the sheet thickness and rolled pancake-shaped grains in inner third. Figure 3(a) presents LM micrographs of the HR cross-section with the measured average grain size and hardness. The average grain size was measured using three circles and two diagonals according to the ASTM E112–13 standard. Usually, the material cools down quicker outside, so it recrystallises more completely in the centre. The fact that the surface areas are recrystallised, while the centre remains mostly deformed may be due to a higher strain introduced into the surface-near regions by the additional shearing caused by roll friction. The uneven grain size distribution most probably results from the uneven temperature distribution across the sample during hot rolling. The texture in the middle is mainly composed of $X1$- and $X2$-fibres and the rotated-Cube, and the texture close to the surface is also mainly composed of $X1$- and $X2$-fibres as well as from η-fibre and with a small addition of Brass and Cube, which indicates the strong shear deformation caused by the friction of the hot-rolling cylinders with the rolled material (Fig. 2). The largest contribution comes from the grains that belong to none of the selected texture components (“random texture”), in the middle and on the surface, i.e., 80% and 61%, respectively. The Brass- and S-oriented grains (bright blue and green in Fig. 2(a)) are mostly flat and elongated, indicating a lack of recrystallisation, in contrast to the grains with other orientations. The surface area is almost completely recrystallised (Fig. 2(b)) compared to middle area where recrystallisation accounted for not more than 30% of the whole volume (Fig. 2(a)), evaluated by using Grain Average Misorientation in OIM software.

3.2 Microstructure

The LM microstructures of hot- and cold-rolled (symmetrically and asymmetrically) and additionally annealed samples are presented in Fig. 3. Compared to the hot-rolled (HR) material, cold-rolling causes a smaller average grain size. However, there is an evident difference between the SCR and ACR grain shape distribution (Figs. 3(b, c)). The middle section with pancake-shaped grains in the SCR material is much larger than that of the ACR sample, where most grains are at least partially recrystallised, and pancake-shaped grains are only present in the very centre of the cross-section. The SCR material has almost 3/4 of pancake-shaped grains, and only the area very close to the surface underwent the recrystallization.

Therefore, the grains in the areas close to the surface are more equiaxed compared to the SCR material. Surprisingly, there is no apparent difference between the surfaces near the faster and slower rollers. During the cold rolling, the hardness increases, but there is no difference between the SCR and ACR samples. The average grain size increases, and the hardness decreases after annealing. Figure 3(d) presents the microstructure of the symmetrically rolled and annealed (SCR+A) sample. The SCR+A sample has a uniform distribution of the average grain size in all three measured positions, which indicates appropriate annealing. Similar to SCR+A, the asymmetrically rolled and annealed (ACR+A) material has an equal hardness in the cross-section. The microstructure of the ACR+A sample is presented in Fig. 3(e) with the measured average grain size and hardness. The grain sizes in both annealed samples are between 19 and 26 μm, resulting in a significantly reduced hardness, compared to the cold rolled samples, of 56 HB at all measured positions.

Details of the microstructure in the middle of the sheets as measured by EBSD are shown in Figs. 4 and 5. The SCR material shows strongly elongated, thin grains, typical for the cold-rolled material. A similar microstructure is observed in the ACR material with a slightly larger number of shear bands distinguished by their 30°−40° inclination to the rolling direction and their strong local orientation changes. A detailed look at Fig. 4(b) (bottom-left corner) reveals grains with crossing shear bands. This phenomenon is not so often seen in the SCR material's microstructure. Thus, based on the microstructures, it appears that shear deformation is more frequent in ACR samples. The annealed materials show a much coarser, clearly recrystallised microstructure. The SCR+A material shows partly equiaxed, recrystallised grains and partly elongated, partly recrystallised or recovered grains, with an aspect ratio of approximately two. A similar recrystallised microstructure is observed in the ACR+A material but with larger grains. The larger grains might be due to the different plastic deformation during the asymmetric cold rolling, which would be reflected in faster recovery and recrystallisation.

Details of the microstructure in areas close to the surface of the sheets as measured by EBSD are shown in Figs. 6 and 7. In the middle of the rolled sample sheet, the grains are pancake-shaped, and the situation close to the surface is different and much less elongated grains are found (Figs. 5(a, b)). The SCR sample on the surface still has some grains elongated across the whole field of view. The ACR sample has, on average, smaller grains, and no very elongated grains can be observed. In both samples, many shear bands are noticeable. During

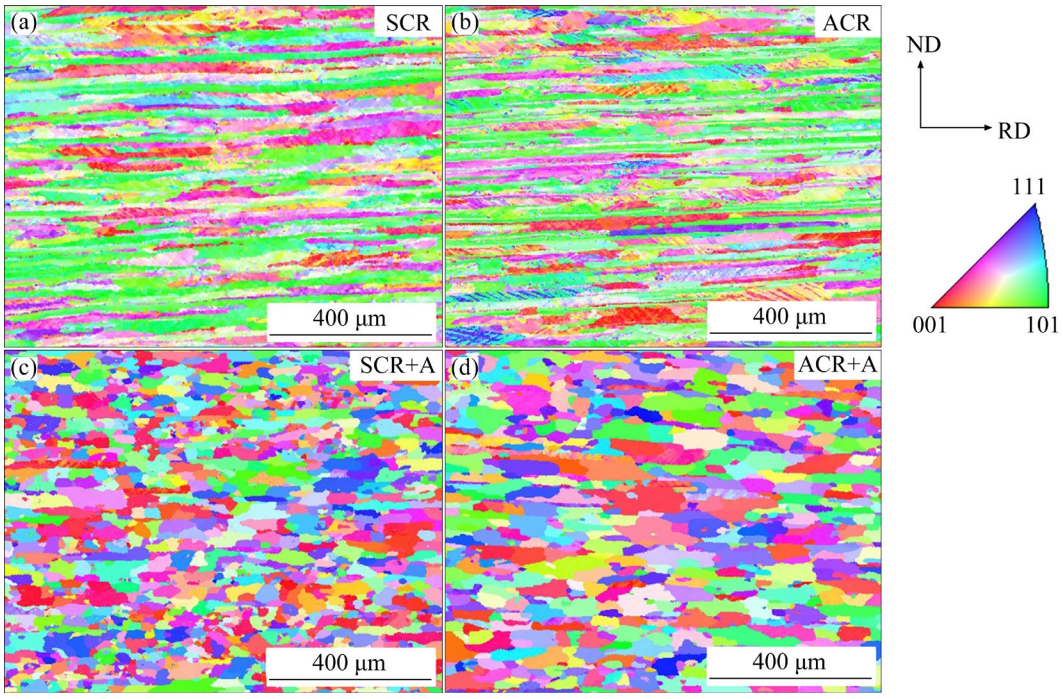

Fig. 4 EBSD IPF-*Z* orientation maps (middle position) of rolled and annealed samples

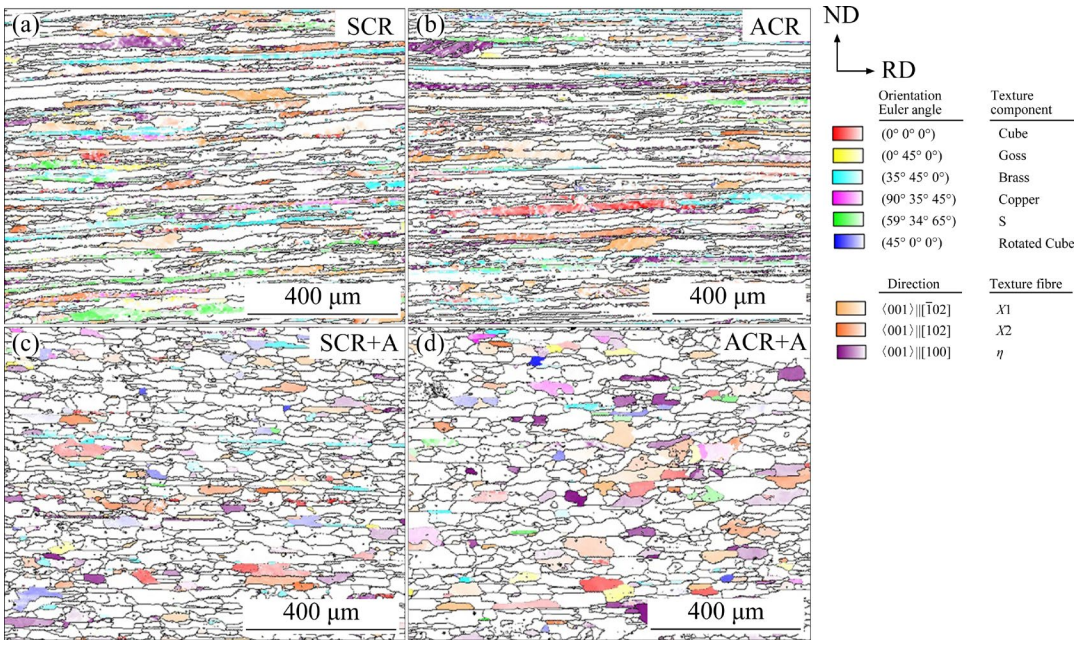

Fig. 5 EBSD-based texture component maps (middle position) of rolled and annealed samples (The colours indicate the spherical and fiber texture components)

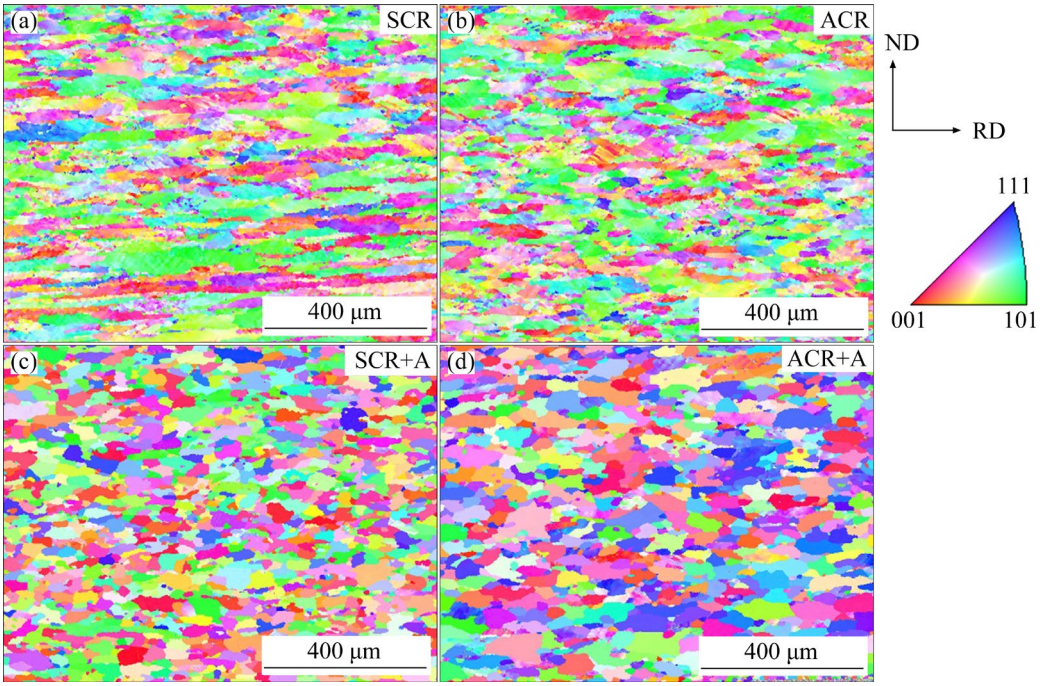

Fig. 6 EBSD IPF-*Z* orientation maps (surface position) of rolled and annealed samples

annealing, the grains completely recrystallised. As observed in the middle, there is no drastic change in grain size from the deformed to the recrystallised structure. However, there is a slight difference in the grain size of the SCR+A compared to the ACR+A sample. Asymmetric rolling leads to slightly larger grains. Again, the reason for the larger grains might be the different plastic deformation during the asymmetric cold rolling, which would be reflected in faster recovery and recrystallisation.

3.3 Crystallographic textures

All the texture results are compiled in Fig. 8 and summarised in Tables 4 and 5, and some texture components and fibres of all the middle and surface

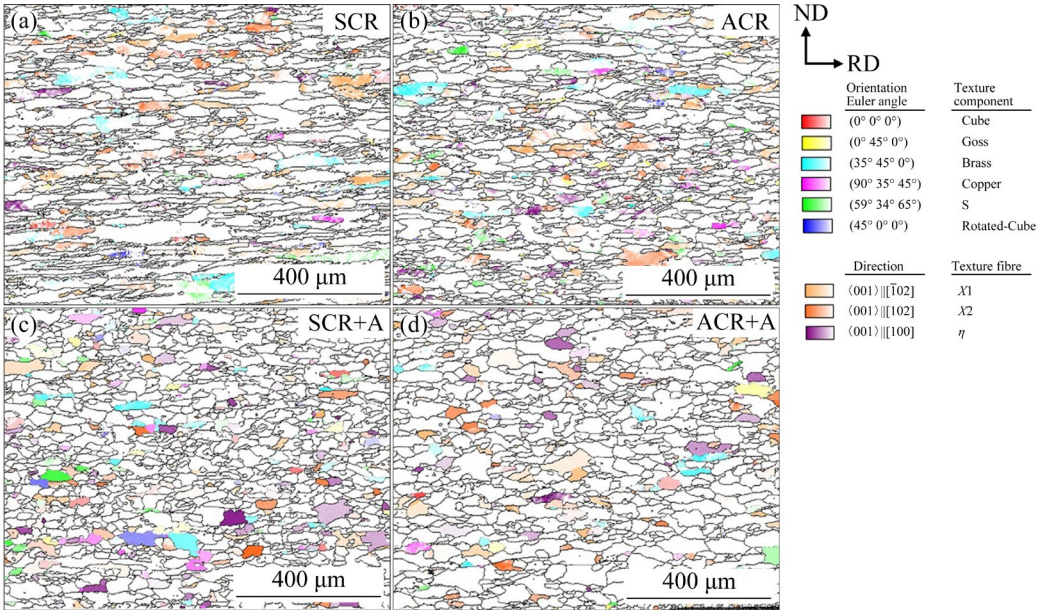

Fig. 7 EBSD-based texture component maps (surface position) of rolled and annealed samples (The colours indicate spherical and fiber texture components)

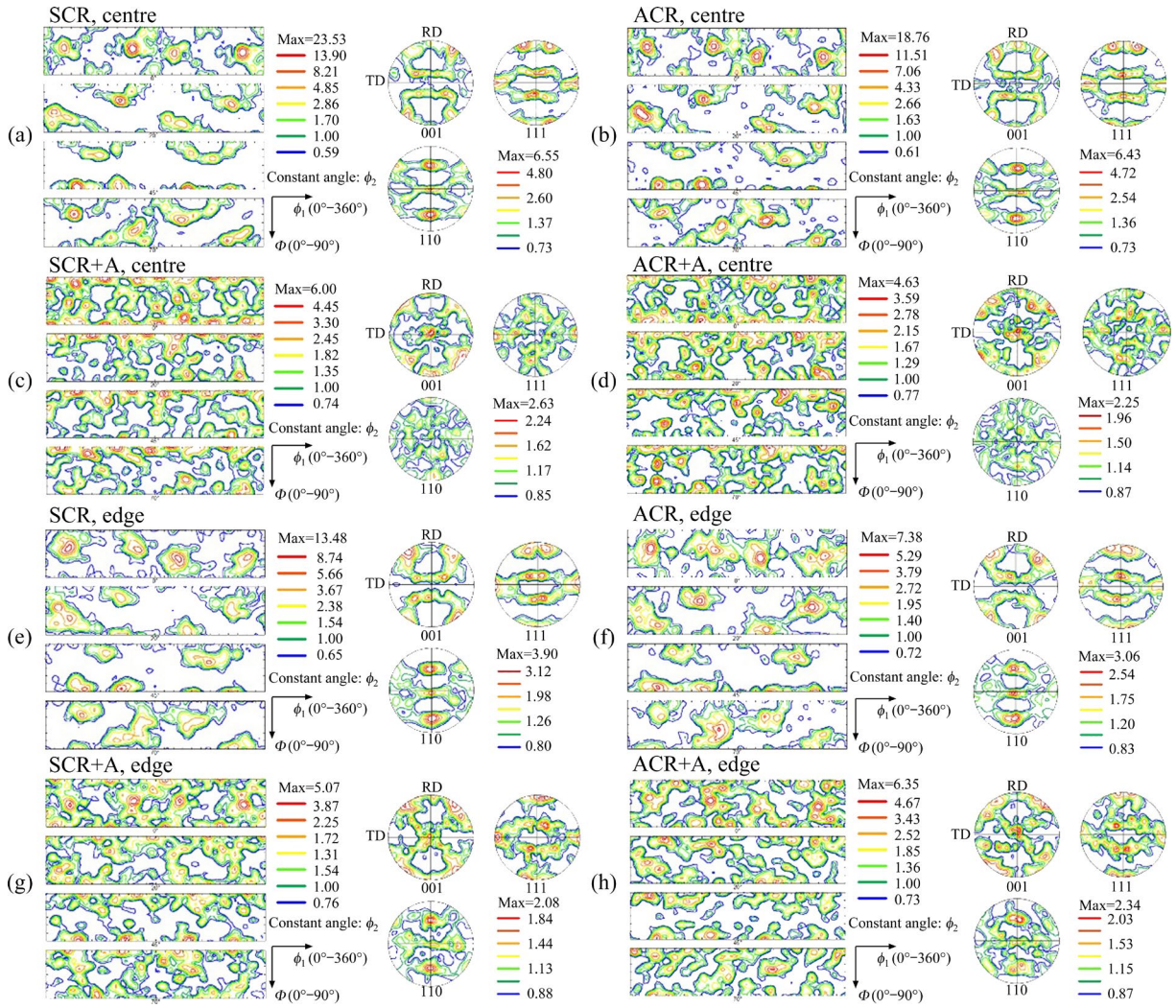

Fig. 8 ODFs and pole-figure textures in middle (a−d) and close to surface (e−h) of sample cross-section

Table 4 Results of SEM−EBSD analysis on textures in middle of sample cross-section

Texture characteristic		Sample				
		HR	SCR	ACR	SCR+A	ACR+A
Max. intensity		15.9	23.5	18.8	7.5	7.7
Volume fraction of spherical texture component/%	Cube	4.0	1.1	2.4	2.1	1.2
	Goss	0.8	1.1	0.6	0.7	0.5
	Brass	5.0	5.1	5.4	2.0	0.9
	Copper	1.0	1.3	0.3	0.8	0.9
	S	2.2	4.8	2.0	0.2	1.6
	Rotated-Cube	0.7	0.1	0.3	2.2	1.4
Volume fraction of fibre texture component/%	$X1$+$X2$-fibre	10.8	14.2	10.1	6.6	9.4
	η-fibre	14.2	6.0	9.2	7.0	5.9
Volume fraction of random/%		61	65	67	79	75

The textures are characterised with the maximum intensity and volume fraction of separate texture components

Table 5 Results of SEM−EBSD analysis on textures close to surface of sample cross-section

Texture characteristic		Sample				
		HR	SCR	ACR	SCR+A	ACR+A
Max. intensity		6.1	13.5	7.4	5.1	6.3
Volume fraction of spherical texture component/%	Cube	0.3	0.5	0.2	1.1	0.7
	Goss	0.3	0.2	1.1	0.9	0.5
	Brass	1.2	4.0	2.7	1.9	1.4
	Copper	0.7	0.4	0.9	1.3	0.5
	S	1.2	1.5	1.5	1.4	0.7
	Rotated-Cube	2.6	0.5	0.4	0.8	0.1
Volume fraction of fibre texture component/%	$X1$+$X2$-fibre	10.6	12.7	11.5	9.3	9.8
	η-fibre	2.3	2.6	4.1	6.2	4.3
Volume fraction of random/%		80	75	76	77	82

The textures are characterised with the maximum intensity and volume fraction of separate texture components

positions are presented in Figs. 5 and 7, respectively. The textures of the initial and differently processed materials show characteristic differences (Figs. 2, 5 and 7). The HR material is the initial material for all the following production steps, and its pole figures are shown in Figs. 2(c, d). In the middle, all three fibres ($X1$, $X2$ and η) form 25 vol.% of all components. The Cube component occupies 4 vol.%, indicating relatively weak pinning of the boundaries by solutes. On the surface, all three fibre components ($X1$, $X2$ and η) form 13 vol.% of all components. The Cube component is almost absent, indicating strong pinning of the boundaries by solutes. Altogether, this texture is typical for a combination of rolling with strong friction and simultaneous recrystallisation.

The conventional SCR material in the middle shows a texture typical for a cold-rolled FCC material with high stacking-fault energy. By far the strongest are the Brass and S components, covering about 10 vol.% of all texture components. As mentioned above, the Brass component is a typical shear component. The $X1$ and $X2$ fibres occupy around 14 vol.%. The crystal orientations are homogeneously distributed. On the surface, the textures are similar but show much less intensity. The ODF plots and pole figures are shown in Figs. 8(a, b).

The texture in the middle of the ACR sheet is different from the SCR material. The ACR texture

intensity is weaker. The ODF and pole figures are shown in Figs. 8(a, b). Compared to the SCR sheet, the S component and the *X*1- and *X*2-fibres are reduced from 5 to 2 vol.% and from 14 to 10 vol.%, respectively, while the Cube and *η*-fibre are increased from 1 to 2 vol.% and 6 to 9 vol.%, respectively. The fact that the grains generally appear slightly larger than the grains in the SCR material could indicate a certain degree of recovery and recrystallisation during the asymmetric rolling process. The temperature can rise significantly due to the strong friction, triggering recrystallisation processes. The texture close to the surface of the ACR sheet is also different from the SCR material. The ODF and pole figures are shown in Figs. 8(e, f). The ACR sheet has slightly weaker *X*1- and *X*2-fibres and a bit stronger *η*-fibre.

The ODFs and related pole figures of the annealed materials, SCR+A and ACR+A in the middle and close to the surface, are shown in Figs. 8(c, d) and 8(g, h), respectively. Generally, the texture sharpness decreases compared to the cold-rolled material. This is to be expected for Al alloys with significant precipitations that pin the grain boundaries or with slowly diffusing alloying elements (e.g., Mn and Cr) that lead to the solute drag of boundaries. These processes prevent the nucleation and growth of new grains with sharp texture components. The SCR+A material in the middle shows a slight increase in the *η*-fibre, a typical recrystallisation fibre, while ACR+A displays a strong decrease in the *η*-fibre. The main difference between SCR and ACR is in the amount of *X*1- and *X*2-fibres. These two fibres together are actually types of fibres that are distributed in the ODF space and occupy most of the volume and, in such a way, contribute to the random texture, which is good for the low earing in a deep-drawability process. Similar observations can be made on the surface of the SCR+A and the ACR+A samples. *X*1- and *X*2-fibres have slightly higher intensity, while the *η*-fibre is weaker after asymmetrical rolling.

Symmetrical and asymmetrical cold rolling also differ with respect to total texture intensity and amount of random texture. The asymmetric rolling randomises the texture and influences the texture intensity.

3.4 Mechanical properties

The results of all the mechanical tests for the cold-rolled samples before and after annealing are presented in Table 6. The hardness values at discrete measurement positions on the cross-section of the different samples are shown in Fig. 3, while the hardnesses in Table 6 are the average values of these measurements. The tensile-test properties and the hardness values are almost the same for the samples ACR and SCR, as well as for the annealed samples ACR+A and SCR+A. As expected, after the annealing, the hardness and the tensile-test values decrease for both the symmetrically and asymmetrically cold-rolled samples. The A_{25mm} and hardness values are precisely the same for the SCR+A and ACR+A, (29±2)% and 56 HB.

In contrast, the results of the plastic-strain-ratio tests differ significantly between the SCR and ACR samples for both the cold-rolled and the annealed states. For the cold-rolled material, the normal anisotropy, r_m, increases from (0.49±0.03) for the SCR to (0.55±0.01) for ACR. However, the opposite trend is observed for annealed material, and r_m drops from (0.62±0.04) for SCR+A to (0.56±0.03) for ACR+A. The planar anisotropy, Δr (it is essential to consider its absolute value) shows similar trends: an increase from SCR to ACR and a decrease from SCR+A to ACR+A.

Table 6 Mechanical properties of symmetric- and asymmetric-rolled samples in deformed (SCR and ACR) as well as annealed conditions (SCR+A and ACR+A)

Sample	Tensile properties			Hardness (HB)	Plastic strain ratio			Earing percentage/%
	R_m/MPa	$R_{p0.2}$/MPa	A_{25mm}/%		Lankford parameter, r	Normal anisotropy, r_m	Planar anisotropy, Δr	
SCR	279±2	230±4	12±2	87±4	0.46±0.05	0.49±0.03	−0.15±0.03	2.17±0.05
ACR	280±1	229±3	12±2	88±5	0.50±0.02	0.55±0.01	−0.20±0.04	2.43±0.04
SCR+A	219±3	89±2	29±2	56±3	0.58±0.04	0.62±0.04	−0.24±0.02	1.62±0.05
ACR+A	218±3	90±1	29±2	56±2	0.53±0.01	0.56±0.03	−0.17±0.02	0.97±0.04

In accordance with the described plastic-strain-ratio results of earing test, the same trend is seen. The SCR sample has (2.17±0.05)% of measured earing, while the ACR sample has a higher percentage of (2.43±0.04)% earing. After the annealing, the earing percentage of the material is decreased. By comparing SCR+A (1.62±0.05)% and ACR+A, the latter has only (0.97±0.04)% of earing. The earing phenomenon is, thus, reduced significantly by almost 60%. This is particularly important, considering that the maximum earing for this material in an industrial application never exceeds 2.5%. The data show that asymmetric rolling has, using texture and microstructure modification, a positive effect on the properties of the annealed material as it reduces its undesirable mechanical anisotropy.

4 Discussion

Even though the differences in the textures of the annealed materials are not significant, the results for earing are very promising for industrial applications. With asymmetric rolling, much less force on the rollers is used, which means a longer life span of rolling mills and considerable energy saving. A rough calculation for rolling-mill energy consumption per working hour for symmetrical and asymmetrical rolling is 3260 and 3050 kW·h, respectively. Therefore, the difference of 210 kW·h of lower electric energy consumption for asymmetric rolling can be greatly beneficial for the aluminium industry.

Table 6 shows that the texture does not significantly influence the fundamental mechanical properties, i.e., yield strength and uniform elongation. These values are mainly determined by the basic composition and the microstructure, i.e., grain size, dislocation density and precipitate content. A difference in grain size between the asymmetrically and symmetrically rolled and annealed samples is visible, but this does not affect the yield strength.

In contrast, the anisotropy values (see HUTCHINSON [27] for a detailed discussion) show differences between the ACR and SCR samples related to the material's texture. Generally, the Lankford parameter, r, indicates the resistance of a material to thinning during stretching operations [28]. For good deformability, particularly in deep drawing, this value should be close to 1 [29]. The normal anisotropy, r_m, is the average of the Lankford parameter for different directions. A large value indicates resistance to thinning for deep-drawing operations with stretching in different directions of a sheet [30]. A high value allows deeper parts to be drawn and is therefore desirable. Finally, the planar anisotropy, Δr, indicates how differently the material deforms in different sheet directions. A large value can lead to strong earing and heterogeneous sheet thicknesses during cup drawing. Conversely, the desirable small absolute value can lead to little earing and homogeneous deep-drawability [27,31].

A synopsis of the values of r, r_m and Δr in Table 6 with the intensities of the texture components in Tables 4 and 5 reveals the following prospects. The sample SCR has the highest texture intensity with only 38 vol.% of "random" orientations, the principal component being the S, Brass and Cube components. At the same time, this sample has the smallest Lankford value, normal anisotropy and the smallest planar anisotropy. During annealing, the sample changes its texture and, consequently, its mechanical behaviour in the opposite direction: the SCR+A sample shows a random texture of 77 vol.% and a well-developed η-fibre with some Cube texture. This sample has, of all samples, a Lankford value close to 1, indicating good deformability, but also the largest absolute planar anisotropy, which would result in strong earing [32].

The asymmetrically rolled samples behave slightly differently from the symmetrically rolled ones. The cold-rolled and the annealed samples have similar texture strengths compared to the asymmetrical ones, but ASCR+A has a higher $X1$- and $X2$-fibres and weaker η-fibre and Cube texture components with higher random texture in the surface. Therefore, this sample should show the best compromise of deep drawability and low earing [33]. Its texture intensity is low, which improves the deep-drawability [34]. At the same time, the components that typically lead to earing, which means components with few symmetric equivalent positions (Cube, Goss, rotated-Cube), are also very low [35].

Asymmetric rolling causes a decrease of η-fibre in the middle and on the aluminium sheet's surface. As a result, the strengthening of the $X1$-

and *X*2-fibres is higher in the middle and on the surface of the aluminium sheet. Asymmetric rolling causes an increase in the material temperature due to higher friction stresses during deformation; therefore, recovery and recrystallisation occur earlier, which is reflected in an increase in the recrystallisation texture (η-fibre).

5 Conclusions

(1) Asymmetric cold rolling leads to different amounts of shear banding in the middle of the aluminium sheet, which, in turn, promotes the formation of the shear fibre textures (*X*1-, *X*2-fibres). Asymmetric cold rolling also causes an increase in the temperature of the material due to friction stresses during deformation; therefore, recovery and recrystallisation occur earlier, which is reflected in an increase in the recrystallisation texture (η-fibre) and larger grains. As a result, grains in the middle generally appear 30% larger, while on the surface the difference is about 10%.

(2) During recrystallisation, the presence of shear bands leads to an effective randomisation of the texture and, therefore, to the low mechanical anisotropy of the asymmetrically rolled material. As a result, the final asymmetric rolling material has fewer Cube, Goss, rotated-Cube and Brass texture components compared to the final symmetric rolled material. These texture components are responsible for earing.

(3) The texture developed after annealing of the asymmetric rolled samples possesses a larger amount of *X*1- and *X*2-fibres, which fairly evenly occupy areas within the ODF space and thus contribute strongly to the weak texture favourable for isotropic properties.

(4) The presence of the η-fibre in the middle and on the surface after asymmetric cold rolling and the fact that the grains generally appear 30% (middle) and 10% (surface) larger could indicate a certain degree of recovery and recrystallisation during the asymmetric rolling process. The temperature can rise significantly due to friction, triggering recrystallisation processes.

(5) The study confirmed that it is possible, with asymmetric rolling involving less rolling force and less energy consumption, to produce a final material with similar or even better mechanical properties in terms of formability, particularly in earing phenomena.

CRediT authorship contribution statement

Matjaž GODEC: Conceptualization, Supervision, Writing − Original draft preparation, Writing − Review & editing; **Stefan ZAEFFERER:** Writing − Review & editing; **Jakob KRANER:** Investigation, Writing − Original draft preparation; **Črtomir DONIK:** Investigation, Writing − Review & editing; **Irena PAULIN:** Investigation, Supervision, Writing − Review & editing.

Declaration of competing interest

The authors declare that they have no known competing financial interests or personal relationships that could have appeared to influence the work reported in this paper.

References

[1] SUWAS S, RAY R K. Crystallographic texture of materials [M]//Engineering Materials and Processes. Springer, 2014.

[2] ENGLER O, LÖCHTE L, HIRSCH J. Through-process simulation of texture and properties during the thermo-mechanical processing of aluminium sheets [J]. Acta Materialia, 2007, 55: 5449−5463.

[3] ZHAO Zi-su, MAO Wei-min, ROTERS F, RAABE D. A texture optimization study for minimum earing in aluminium by use of a texture component crystal plasticity finite element method [J]. Acta Materialia, 2004, 52: 1003−1012.

[4] HIRSCH J. Texture evolution during rolling of aluminium alloys [J]. Light Metals, 2008: 1071−1077.

[5] MISHRA S, KULKARNI K, GURAO N P. Effect of crystallographic texture on precipitation induced anisotropy in an aluminium magnesium silicon alloy [J]. Materials & Design, 2015, 87: 507−519.

[6] ZHAO Qi, LIU Zhi-yi, HUANG Tian-tian, XIA Peng, LI Fu-dong. Enhanced fracture toughness in an annealed Al−Cu−Mg alloy by increasing Goss/Brass texture ratio [J]. Materials Characterization, 2016, 119: 47−54.

[7] JAMAATI R, TOROGHINEJAD M R. Effect of alloy composition, stacking fault energy, second phase particles, initial thickness, and measurement position on deformation texture development of nanostructured FCC materials fabricated via accumulative roll bonding process [J]. Materials Science and Engineering A, 2014, 598: 77−97.

[8] JAZAERI H, HUMPHREYS F J. The transition from discontinuous to continuous recrystallization in some aluminium alloys. I: The deformed state [J]. Acta Materialia, 2004, 52: 3239−3250.

[9] PAPADOPOULOU S, KONTOPOULOU A, GAVALAS E, PAPAEFTHYMIOU S. The effects of reduction and thermal treatment on the recrystallization and crystallographic texture evolution of 5182 aluminum alloy [J]. Metals (Basel), 2020,

10: 1380.

[10] SIDOR J, MIROUX A, PETROV R, KESTENS L. Microstructural and crystallographic aspects of conventional and asymmetric rolling processes [J]. Acta Materialia, 2008, 56: 2495−2507.

[11] DONG Hai-peng, GUO Fei, HUANG Wei-jiu, YANG Xu-sheng, ZHU Xiang-hui, LI Hu, JIANG Lu-yao. Shear banding behavior of AA2099 Al−Li alloy in asymmetrical rolling and its effect on recrystallization in subsequent annealing [J]. Mater Characterization, 2021, 177: 111155.

[12] WEI Yi-li, GODFEY A, LIU Wen-jia, LIU Qing, HUANG Xiao-xu, HANSEN N, WINTHER G. Dislocations, boundaries and slip systems in cube grains of rolled aluminium [J]. Scripta Materialia, 2011, 65: 355−358.

[13] LEFFERS T, RAY R K. The brass-type texture and its deviation from the copper-type texture [J]. Progress in Materials Science, 2009, 54: 351−396.

[14] WANG Xiao-feng, GUO Ming-xing, ZHANG Yan, XING Hui, LI Yong, LUO Jin-ru, ZHANG Ji-shan, ZHUANG Lin-zhong. The dependence of microstructure, texture evolution and mechanical properties of Al−Mg−Si−Cu alloy sheet on final cold rolling deformation [J]. Journal of Alloys and Compounds, 2016, 657: 906−916.

[15] HIRSCH J, AL-SAMMAN T. Superior light metals by texture engineering: Optimized aluminum and magnesium alloys for automotive applications [J]. Acta Materialia, 2013, 61: 818−843.

[16] ZAEFFERER S, BAUDIN T, PENELLE R. A study on the formation mechanisms of the cube recrystallization texture in cold rolled Fe−36%Ni alloys [J]. Acta Materialia, 2001, 49: 1105−1122.

[17] LI Sha-sha, ZHAO Qi, LIU Zhi-yi, LI Fu-dong. A review of texture evolution mechanisms during deformation by rolling in aluminum alloys [J]. Journal of Materials Engineering and Performance, 2018, 27: 3350−3373.

[18] INOUE H, TAKASUGI T. Texture control for improving deep drawability in rolled and annealed aluminum alloy sheets [J]. Materials Transactions, 2007, 48: 2014−2022.

[19] ENGLER O, KIM H C, HUH M Y. Formation of {111} fibre texture in recrystallised aluminium sheet [J]. Materials Science and Technology, 2001, 17: 75−86.

[20] KRANER J, FAJFAR P, PALKOWSKI H, KUGLER G, GODEC M, PAULIN I. Microstructure and texture evolution with relation to mechanical properties of compared symmetrically and asymmetrically cold rolled aluminum alloy [J]. Metals (Basel), 2020, 10: 156.

[21] DUTTA S, KAISER M S. Effect of asymmetric rolling on formability of pure aluminium [J]. Journal of Mechanical Engineering, 2014, 44: 94−99.

[22] ZUO Fang-qing, JIANG Jian-hua, SHAN Ai-dang, FANG Jian-min, ZHANG Xing-yao. Shear deformation and grain refinement in pure Al by asymmetric rolling [J]. Transactions of Nonferrous Metals Society of China, 2008, 18: 774−777.

[23] ŠIMČAK D, KVAČKAJ T, KOČIŠKO R, BIDULSKY R, KEPIČ J, PUCHY V. Evaluation of high purity aluminium after asymmetric rolling at ambient and cryogenic temperatures [J]. Acta Metallurgica Slovaca, 2017 23: 99−104.

[24] ZANCHETTA B D, DA SILVA V K, SORDI V L, RUBERT J B, KLIAUGA A M. Effect of asymmetric rolling under high friction coefficient on recrystallization texture and plastic anisotropy of AA1050 alloy [J]. Transactions of Nonferrous Metals Society of China, 2019, 29: 2262−2272.

[25] van HOUTTE P, SHORE D, van BAEL A. Study of asymmetric rolling to improve textures and r-values of aluminium deep drawing alloys [J]. Materials Science Forum, 2018, 941: 1330−1335.

[26] JEONG H B, NAM S K, LEE J H, KIM G H, KIM I. Deep drawability improvement of two steps asymmetrically rolled and heat-treated AA7075 Al alloy sheet [J]. Materials Research Innovations, 2015, 19: 584−588.

[27] HUTCHINSON B. Anisotropy in metals [J]. Materials Science and Technology, 2015, 31: 1393−1401.

[28] WRONSKI S, WROBEL M, BACZMANSKI A, WIERZBANOWSKI K. Effects of cross-rolling on residual stress, texture and plastic anisotropy in f.c.c. and b.c.c. metals [J]. Materials Characterization, 2013, 77: 116−126.

[29] JAIN M, ALLIN J, BULL M J. Deep drawing characteristics of automotive aluminum alloys [J]. Materials Science and Engineering A, 1998, 256: 69−82.

[30] WIDIANTARA P I, YANG H W, KIM Min-jun, KO Young-gun. Plastic anisotropy calculation of severely-deformed Al−Mg−Si alloy considering texture changes in electron backscatter diffraction [J]. Journal of Materials Science & Technology, 2019, 35: 1439−1443.

[31] DUAN Xiao-ge, JIANG Hai-tao, MI Zhen-li, CHENG Lei, WANG Jia-yi. Reduce the planar anisotropy of AA6016 aluminum sheets by texture and microstructure control [J]. Crystals (Basel), 2020, 10: 1027.

[32] HIRSCH J. Texture evolution and earing in aluminium can sheet [J]. Materials Science Forum, 2005, 495: 1565−1572.

[33] VINCZE G, SIMOES F J P, BUTUC M C. Asymmetrical rolling of aluminum alloys and steels: A review [J]. Metals (Basel), 2020, 10: 1126.

[34] AMIRI M M, FERESHTEH-SANIEE F. Influence of roll speed difference on microstructure, texture and mechanical properties of 7075 aluminum plates produced via combined continuous casting and rolling process [J]. Transactions of Nonferrous Metals Society of China, 2021, 31: 901−912.

[35] LUO Kai-guang, WU Yu-ze, XIONG Han-qing, ZHANG Yun, KONG C, YU Hai-liang. Enhanced mechanical properties of aluminum matrix composites reinforced with high-entropy alloy particles via asymmetric cryorolling [J]. Transactions of Nonferrous Metals Society of China, 2023, 33: 1988−2000.

对称和不对称轧制对加工硬化 AA 5xxx 铝合金织构演化的影响

Matjaž GODEC[1], Stefan ZAEFFERER[2], Jakob KRANER[1,3], Črtomir DONIK[1], Irena PAULIN[1]

1. Institute of Metals and Technology, Lepi pot 11, 1000, Ljubljana, Slovenia;
2. Max-Planck-Institut für Eisenforschung, Max-Planck-Strasse 1, 40237 Düsseldorf, Germany;
3. Impol 2000 d.d., Partizanska cesta 38, 2310 Slovenska Bistrica, Slovenia

摘　要：研究了热轧和冷轧 AA 5454 铝合金板材的织构和显微组织，特别比较了对称和不对称冷轧过程中织构的发展。采用扫描电子显微镜结合电子背散射衍射技术监测不同变形方式及退火样品的显微组织演变。观察并讨论了轧制过程中单个织构组分的形成和转变。解释了对称和不对称冷轧样品的平均晶粒尺寸、织构和力学性能的相互关系。由于不对称轧制能够减少立方、高斯、旋转立方和 η 纤维等织构组分，从而降低退火材料的平面各向异性，因此有利于提高深冲性能。同时，不对称轧制还能够增强 $X1$ 和 $X2$ 纤维状剪切织构组分，从而提高深冲性能。在不对称冷轧过程中，由于摩擦导致温度升高，引发再结晶，导致晶粒长大。研究证实不对称冷轧所需的轧制力更小，因而能够消耗更少的能量生产出具有更好成形性、尤其是更小制耳的最终材料。

关键词：晶体学织构；EBSD；铝合金；对称/不对称轧制；各向异性

(Edited by Bing YANG)